Weilin Qu

Issam Mudawar[1]
e-mail: mudawar@ecn.purdue.edu

Boiling and Two-Phase Flow Laboratory,
School of Mechanical Engineering,
Purdue University,
585 Purdue Mall,
West Lafayette, IN 47907-2088

Sang-Youp Lee

Steven T. Wereley

Microfluidics Laboratory,
School of Mechanical Engineering,
Purdue University,
585 Purdue Mall,
West Lafayette, IN 47907-2088

Experimental and Computational Investigation of Flow Development and Pressure Drop in a Rectangular Micro-channel

Flow development and pressure drop were investigated both experimentally and computationally for adiabatic single-phase water flow in a single 222 μm wide, 694 μm deep, and 12 cm long rectangular micro-channel at Reynolds numbers ranging from 196 to 2215. The velocity field was measured using a micro-particle image velocimetry system. A three-dimensional computational model was constructed which provided a detailed description of liquid velocity in both the developing and fully developed regions. At high Reynolds numbers, sharp entrance effects produced pronounced vortices in the inlet region that had a profound influence on flow development downstream. The computational model showed very good predictions of the measured velocity field and pressure drop. These findings prove the conventional Navier-Stokes equation accurately predicts liquid flow in micro-channels, and is therefore a powerful tool for the design and analysis of micro-channel heat sinks intended for electronic cooling. [DOI: 10.1115/1.2159002]

Introduction

Hydrodynamic and thermal transport aspects of liquid flow in micro-channels with characteristic dimensions from 10 to 1000 μm are of considerable interest to many emerging technologies. One application that is of particular interest to the electronics community is thermal management of high-power-density microprocessors. Micro-channel flow has recently been widely identified as a prime contender for cooling of next generation cutting-edge electronics [1].

Micro-channel flow is achieved inside a specialized heat sink that is attached to the surface of an electronic device. Typically fabricated from a high-thermal-conductivity solid substrate such as copper or silicon, a micro-channel heat sink contains a series of parallel micro-channels that serve as flow passages for the liquid coolant. The heat generated by the electronic device is transferred by conduction to the micro-channels through the solid substrate of the heat sink, and carried away from the heat sink by the liquid flowing through the micro-channels.

Micro-channel heat sinks are capable of dissipating large amounts of heat from small areas. The merits of liquid flow in small channels and micro-channel heat sinks were first conceived for gas turbine blade cooling applications [2,3]. The same concept was proposed for electronic cooling by Tuckerman and Pease [4], who used chemical etching to form parallel rectangular micro-channels (50 μm wide by 302 μm deep, and separated by 50 μm walls) in a 1 cm^2 silicon wafer. Using water as a coolant, their heat sink was capable of dissipating 790 W/cm^2 with a maximum substrate temperature rise of 71°C above the water inlet temperature and a pressure drop of 2.2 bar. Several experimental studies followed Tuckerman and Pease's work, where micro-channel heat sinks with different solid substrates, channel geometries, dimensions, and cooling liquids were fabricated and tested [5–9]. These studies further demonstrated the merits of micro-channel heat sinks for electronic cooling: very small convective thermal resistance, large surface area to volume ratio, small heat sink mass and volume, and small coolant inventory.

The design of a micro-channel heat sink requires accurate depiction of micro-channel flow. Two approaches are commonly used to describe fluid flow and heat transfer in micro-channel heat sinks. The first employs simplified analytical methods [10–13], assuming the solid walls separating micro-channels behave as thin fins, and relying on such approximations as uniform fluid temperature, one-dimensional heat transfer, and constant convective heat transfer coefficient along the micro-channel walls, evaluated from empirical heat transfer correlations. The other approach involves solving the three-dimensional Navier-Stokes and energy equations [14,15].

Both of these approaches are based on prior understanding of fluid flow and heat transfer in macro-channels, and are therefore valid only if liquid flow in micro-channels follows the same conservation laws as in macro-channels. Several studies have been conducted to explore this important fundamental issue. Most of these studies relied on bulk flow measurements, comparing pressure drop measurements across the channel to macro-channel model/correlation predictions. The results show significant disagreements. Some studies showed the measured pressure drop is higher [16–19] or lower [20–22] than the macro-channel model/correlation predictions, while others indicated macro-channel models/correlations adequately describe micro-channel flow [23–25].

Single-phase liquid flow in a channel with a constant cross section can be divided into two regions: a developing region, where the velocity profile changes from some initial profile to an invariant one downstream, and a fully developed region, where the velocity profile is independent of stream-wise distance. For laminar flow in a rectangular channel with a uniform velocity profile at the inlet, the length of the developing region has been discussed in detail by Shah and London [26] and approximated by

$$L_d = (0.06 + 0.07\beta - 0.04\beta^2)\text{Re}_{ch}d_h \qquad (1)$$

where β, Re_{ch}, and d_h are the channel aspect ratio, Reynolds number, and channel hydraulic diameter, respectively. Since micro-channel heat sinks are typically used in high-heat-flux applications, a relatively large liquid flow rate is required to maintain a

---

[1]To whom correspondence should be addressed.
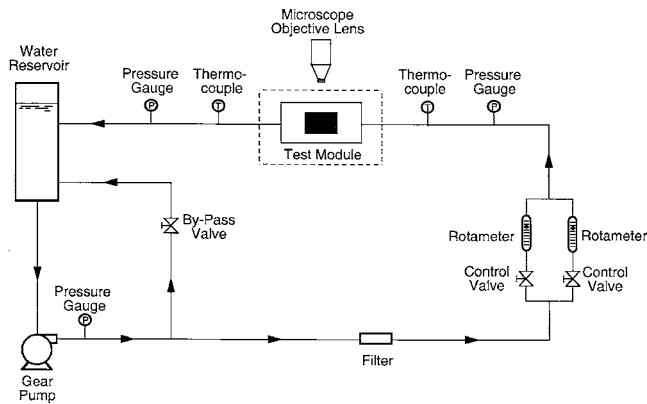
Fig. 1 Schematic of flow loop

small stream-wise temperature rise in both the heat sink and electronic device. Even through micro-channels possess very small cross-sectional dimensions, a large flow rate can result in developing regions that are comparable to, if not larger than, the entire micro-channel. Understanding the developing flow behavior in a micro-channel is therefore vital to understanding the cooling performance of a micro-channel heat sink. This is clearly evident is a recent study by Qu and Mudawar [27] which revealed that empirical heat transfer correlations that account for entrance effects
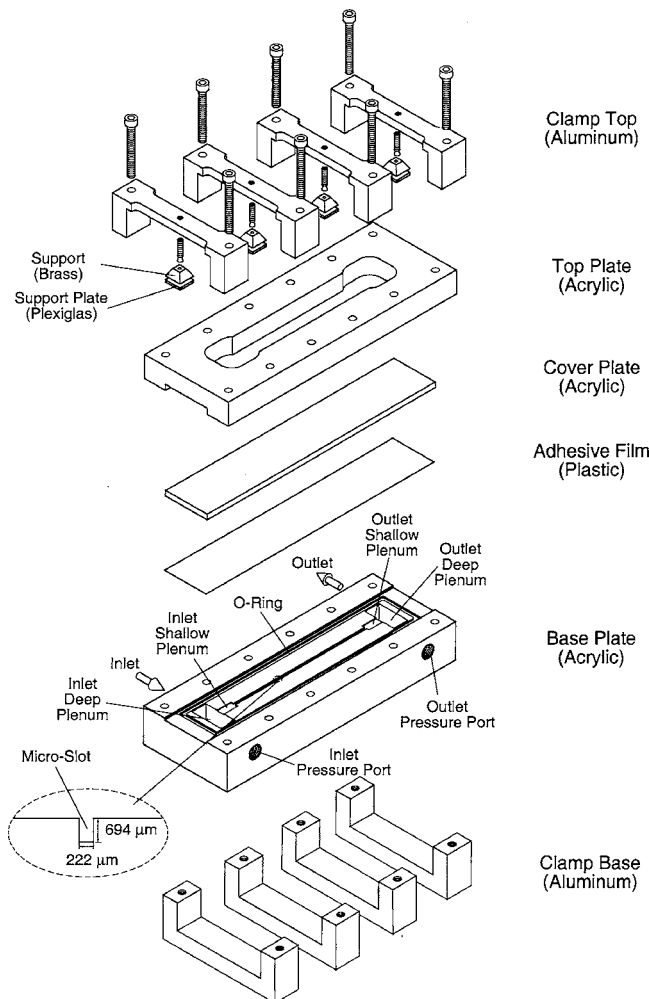
provide fairly accurate predictions of the cooling performance of a micro-channel heat sink, while those utilizing fully developed flow correlations show appreciable error.

In this study, adiabatic flow development of water in a rectangular micro-channel is investigated both experimentally and computationally. The local velocity field was measured by a micro-particle image velocimetry (micro-PIV) system. The experimental results are compared to computational predictions to assess the suitability of macro-transport models to depicting the transport characteristics of developing micro-channel flow. A detailed description of the development behavior is presented and discussed. The results provide fundamental insight into the complex three-dimensional characteristics of micro-channel developing flow. Finally, predictions based on the three- dimensional computational model are compared to pressure drop data.

This study constitutes a crucial step towards validating the conventional Navier-Stokes equation for complex three-dimensional hydrodynamically developing liquid flows in micro-scale channels. This validation represents a necessary precursor to any thermal analysis of a micro-channel heat sink.

Experimental Apparatus

Flow Loop. Figure 1 shows a schematic of the flow loop that was constructed to supply deionized water to a micro-channel test module at room temperature. The water was circulated through the flow loop from a reservoir with the aid of a variable speed gear pump. The flow first passed through a filter to prevent solid particles from blocking the micro-channel. The water then entered one of two rotameters for volume flow rate measurement. The rotameters were calibrated at different water temperatures using the standard weighting method, and their measurement accuracy was better than 4%. After the flow rate measurement, the water flowed through the micro-channel test module where the velocity field and pressure drop were measured using a micro-PIV system and pressure transducers, respectively. Exiting the test module, the water returned to the reservoir. Two thermocouples were installed both upstream and downstream of the test module to measure the water temperature that was used for determination of thermo-

Fig. 2 Construction of micro-channel test module
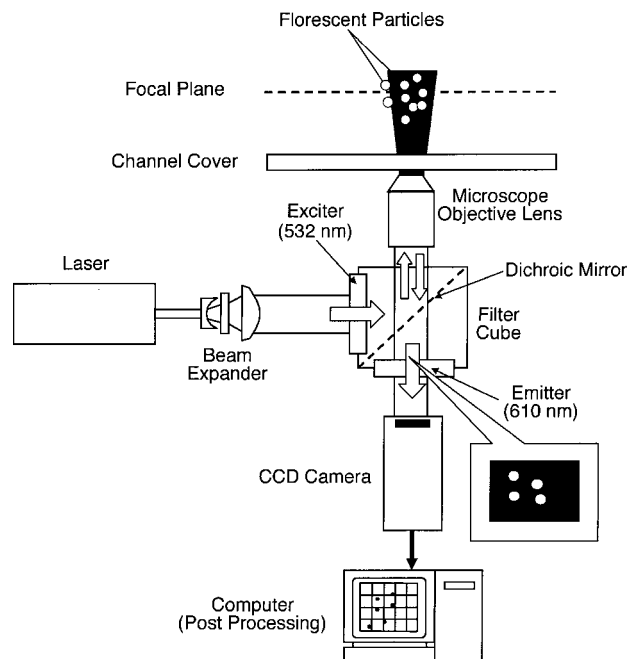
Fig. 3 Schematic of micro-PIV system
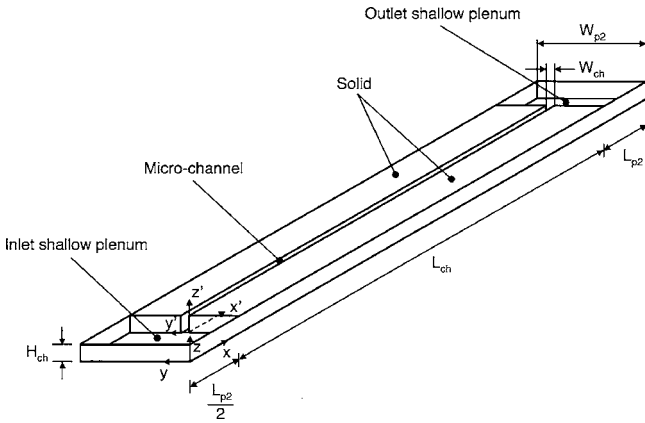
Fig. 4 Computational domain

physical properties. Several pressure gauges were incorporated throughout the flow loop to aid the operator in monitoring the system pressure.

Test Module. Figure 2 illustrates the key components of the micro-channel test module: a base plate, a thin plastic adhesive film, a cover plate, a top (support) plate, and four sets of clamps. The based plate, cover plate, and top plate were all fabricated from transparent acrylic to facilitate optical and visual access to the flow within the micro-channel. A rectangular 222 μm wide, 694 μm deep, and 120 mm long micro-slot was machined into the top surface of the base plate by a precision saw. The 25.4 μm thick transparent adhesive plastic film (Adhesive Research Inc.) has an optical transmission rate over 95%. It was taped down to the 1.6 mm thick cover plate that was pressed against the base plate with the aid of the four clamps to form a closed micro-channel. The top plate was hollowed out in the middle so that the

microscope objective lens of the micro-PIV system could be brought to within a very short distance from the flow. An O-ring in the base plate maintained a leak-proof assembly.

The base plate contained deep plenums leading to shallow plenums both upstream and downstream of the micro-channel. The shallow plenums were 6.35 mm wide, 694 μm deep, and 12.7 mm long. Two absolute pressure transducers were connected to the base plate's deep plenums to measure the inlet and outlet pressures. The pressure transducers were calibrated against a known standard and their measurement uncertainty was less than 3.5%. Pressure drop across the micro-channel was determined from the measured inlet and outlet pressures

$$\Delta P_{exp} = P_{in} - P_{out} \qquad (2)$$

The pressure drop measurements were conducted at Reynolds numbers of 196, 1021, 1895, and 2215.

Micro-PIV System. Figure 3 shows a schematic of the micro-PIV system that was used to measure the velocity field in the developing and fully developed regions along the micro-channel. A brief overview of the micro-PIV system is given below; further

Table 1 Dimensions of micro-channel computational domain

W_{ch} (μm)	H_{ch} (μm)	L_{ch} (mm)	W_{p2} (mm)	L_{p2} (mm)
222	694	120	6.35	12.7

(a)
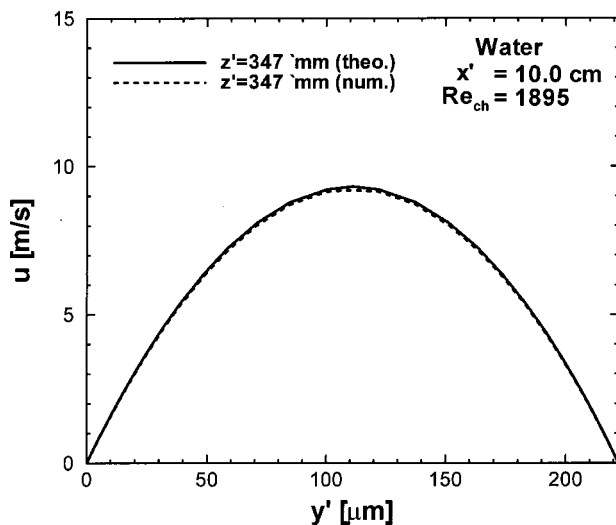
Fig. 5 Comparison of numerical predictions of horizontal middle-plane ($z' = 347$ μm) velocity profile for $Re_{ch} = 1895$ at $x' = 10$ cm with analytical fully-developed profile
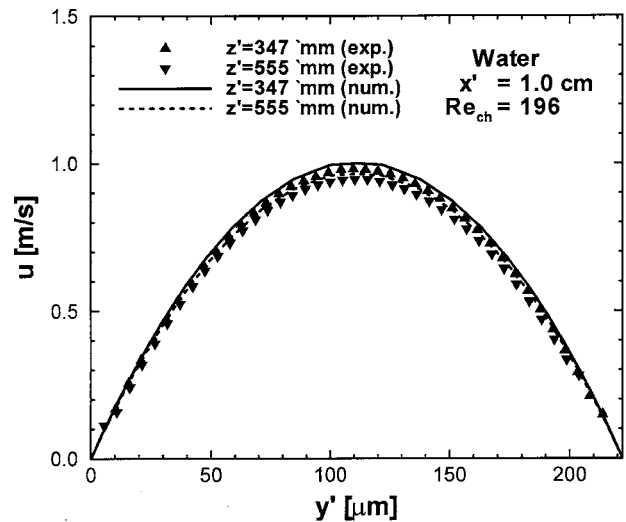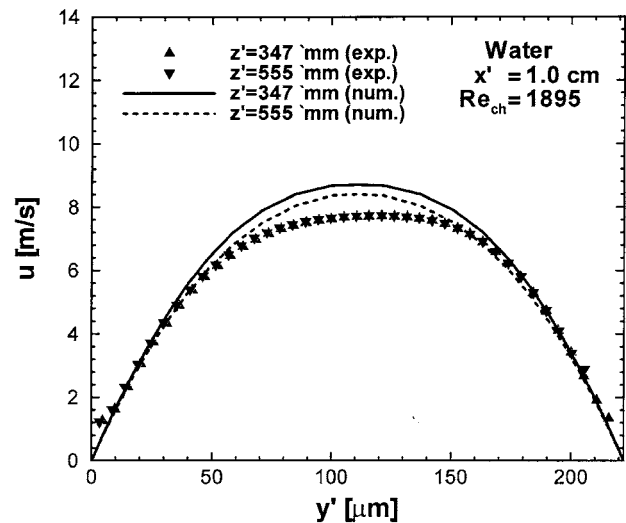
(b)

Fig. 6 Comparison of measured with numerically predicted velocity profiles at two horizontal planes ($z' = 347$ μm and $z' = 555$ μm) and $x' = 1$ cm for (a) $Re_{ch} = 196$ and (b) $Re_{ch} = 1895$

details are available in Ref. [28].

The micro-PIV system is composed of three major components: a two-cavity frequency-doubled Nd:yttrium-aluminum-garnet (YAG) laser (New Wave Inc.), an inverted epi-fluorescent microscope (Nikon TE200), and an interline transfer charge coupled device (CCD) camera (LaVision Inc.). The laser is used for illumination. The wavelength and pulse width of the laser beam are 532 nm and about 3–5 ns, respectively. A beam expander assembly is installed between the laser and the microscope to match the quality of the laser beam to that of the white light source. The beam expander is configured with a negative and a positive lens in a Galilean telescope arrangement, and a 5 deg diffuser is situated between the two lenses to preclude damage to the internal optics of the microscope.

After passing through the beam expander assembly, the laser beam enters the microscope. The microscope consists of an epi-fluorescence filter cube and an objective lens. As illustrated in Fig. 3, the filter cube consists of an exciter (green filter), an emitter (red filter), and a dichroic mirror. After passing through the exciter, the incoming laser beam reaches the dichroic mirror, which is designed to reflect short-wavelengths ($\lambda < 610$ nm) and transmit long ones. The laser beam ($\lambda \sim 532$ nm) is therefore redirected to the objective lens.

The laser beam coming out from the objective lens was used to illuminate the flow field in the micro-channel. Fluorescent particles about 1 μm in diameter were suspended in the flow and served as seeding particles, absorbing the illuminating laser beam ($\lambda \sim 532$ nm, green) and emitting the longer wavelength light ($\lambda \sim 610$ nm, red). The light emitted from the seeding particle carried the image of the flow field. The light passed through the objective lens, dichroic mirror, emitter, and eventually reached the CCD camera. After a specified time delay, the same process was repeated to acquire a second image of the flow field. The velocity field was obtained from the two images using cross-correlation based interrogation [28].

In the present study, the micro-PIV measurements of local velocity field were performed at Reynolds numbers of 196 and 1895. The uncertainty in these measurements is less than 1%.

Computational Model

Figure 4 shows the computational domain that was adopted for analysis of flow development and pressure drop in the micro-channel. The computational domain contained half of the inlet shallow plenum, the micro-channel, the entire outlet shallow plenum, and two solid regions adjoining the micro-channel.

As illustrated in Fig. 4, two coordinate systems were employed: an x-y-z coordinate system that was applied to the entire computational domain, and an x'-y'-z' system that was used to describe the flow field in the micro-channel alone. Dimensions of the computational domain are given in Table 1.

The following assumptions were adopted before applying differential conservation equations to the computational domain

(1) steady flow
(2) incompressible fluid
(3) laminar flow
(4) constant solid and fluid properties

For the water flow in the micro-channel as well as the inlet and outlet shallow plenums, the above assumptions reduce the continuity and momentum equations, respectively, to the following

$$\nabla \vec{V} = 0 \tag{3}$$

$$\text{and } \rho_f(\vec{V} \cdot \nabla \vec{V}) = -\nabla P + \mu_f \nabla^2 \vec{V} \tag{4}$$

For the solid regions, the continuity and momentum equations are simply

$$\vec{V} = 0 \tag{5}$$

The boundary conditions for the computational domain were specified as follows. As indicated in Fig. 4, the inlet of the computational domain was located half-way along the inlet shallow plenum, where the flow was assumed fully developed. A fully-developed velocity profile [26] was therefore applied at the computational domain inlet

$$u = u_{p2,\text{in},m} \frac{48 \sum\limits_{n=1,3,\ldots}^{\infty} \frac{(-1)^{(n-1)/2}}{n^3} \left\{ 1 - \frac{\cosh\left(n\pi \left| z - \frac{H_{\text{ch}}}{2} \right| / W_{p2} \right)}{\cosh[n\pi H_{\text{ch}}/(2W_{p2})]} \right\} \cos\left(\frac{n\pi \left| y - \frac{W_{p2}}{2} \right|}{W_{p2}} \right)}{\pi^3 \left\{ 1 - \frac{192}{\pi^5} \left(\frac{W_{p2}}{H_{\text{ch}}} \right) \sum\limits_{n=1,3,\ldots}^{\infty} \frac{1}{n^5} \tanh\left(\frac{n\pi H_{\text{ch}}}{2W_{p2}} \right) \right\}}$$

$$v = 0, \quad w = 0 \tag{6}$$

for $x = 0$, $0 \leqslant y \leqslant W_{p2}$, and $0 \leqslant z \leqslant H_{\text{ch}}$

where $u_{p2,\text{in},m}$ is the mean velocity in the inlet shallow plenum

$$u_{p2,\text{in},m} = \frac{\dot{V}_{\text{exp}}}{A_{p2}} \tag{7}$$

The flow was assumed fully developed at the computational domain outlet

$$\frac{\partial u}{\partial x} = 0, \quad \frac{\partial v}{\partial x} = 0, \quad \frac{\partial w}{\partial x} = 0 \tag{8}$$

for $x = L_{ch} + \dfrac{3L_{p2}}{2}$, $0 \leqslant y \leqslant W_{p2}$, and $0 \leqslant z \leqslant H_{\text{ch}}$.

The velocity is zero along all other boundaries.

The governing differential equations, Eqs. (3)–(5), together with the above boundary conditions, were discretized along the x, y, and z coordinates using the finite difference method, which resulted in a system of algebraic equations. The grid system for the entire computational domain had 262, 81, and 51 nodes in the x, y, and z directions, respectively. The micro-channel itself con-
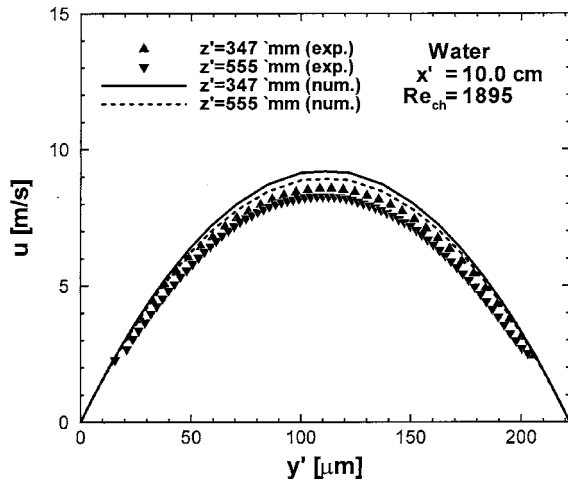
Fig. 7 Comparison of measured with numerically predicted velocity profiles at two horizontal planes ($z' = 347$ μm and $z' = 555$ μm) and $x' = 10$ cm for $Re_{ch} = 1895$

Fig. 8 Comparison of measured with numerically predicted central line velocities along stream-wise direction for $Re_{ch} = 196$ and 1895

tained $160 \times 39 \times 51$ nodes in the x', y', and z' directions, respectively. A nonuniform grid consisting of a larger number of grid points near the channel inlet and outlet as well as the channel walls was employed to better resolve the velocity field. The SIMPLE algorithm [29] was used to solve the resulting system of algebraic equations in primitive variables, namely u, v, w, and P. When solving the momentum equations, water viscosity was evaluated at the average of the measured inlet and outlet temperatures. This viscosity value was used throughout the micro-channel and shallow plenums. A very large viscosity value was assigned to the solid, essentially yielding zero velocity throughout the solid regions. The Gauss-Seidel iterative technique was employed in the solution process, with successive over-relaxation to improve convergence time. The solution was considered convergent when the

criterion $\max \left| (\phi^{\tau+1} - \phi^{\tau}) / \phi^{\tau+1} \right| \leq 10^{-4}$ was satisfied, where ϕ represents any velocity component, namely u, v, or w, and τ is the iteration number.

The computational code was verified by comparing the results with available analytical solutions. Figure 5 shows numerical predictions for the horizontal middle-plane velocity profile (at $z' = H_{ch}/2 = 347$ μm) near the micro-channel exit ($x' = 10$ cm) at $Re_{ch} = 1895$ are in excellent agreement with the analytical fully-developed velocity profile [26]. The micro-channel Reynolds number Re_{ch} is defined as
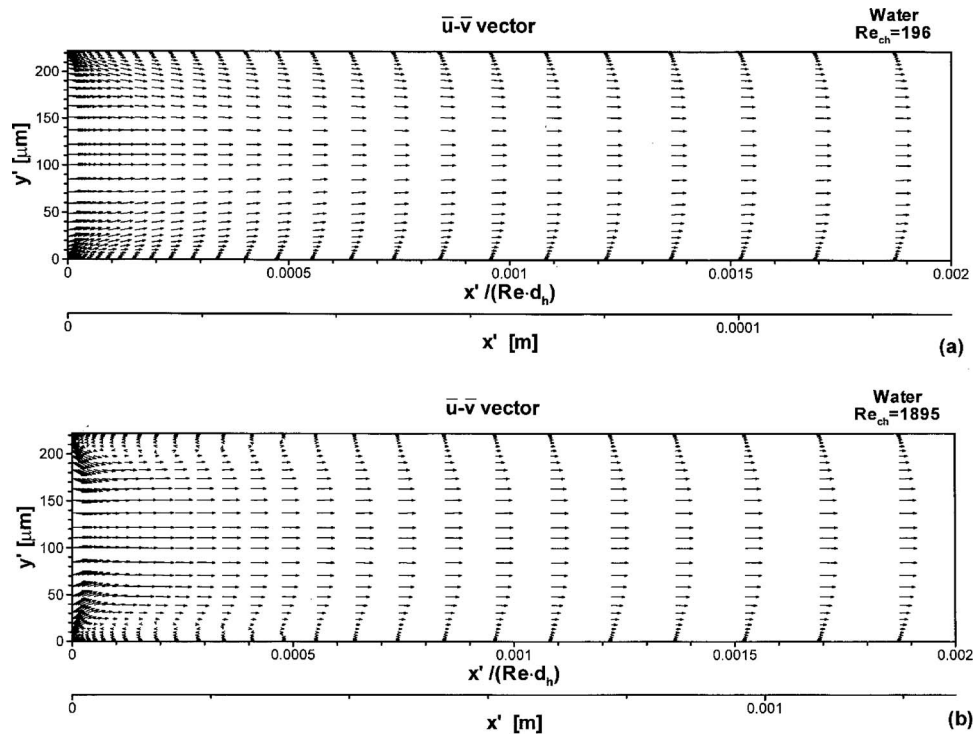
Fig. 9 $\bar{u}$-$\bar{v}$ vector fields at horizontal middle-plane ($z' = 347$ μm) and $0 \leq x'/(Re_{ch}d_h) \leq 0.002$ for (a) $Re_{ch} = 196$ and (b) $Re_{ch} = 1895$
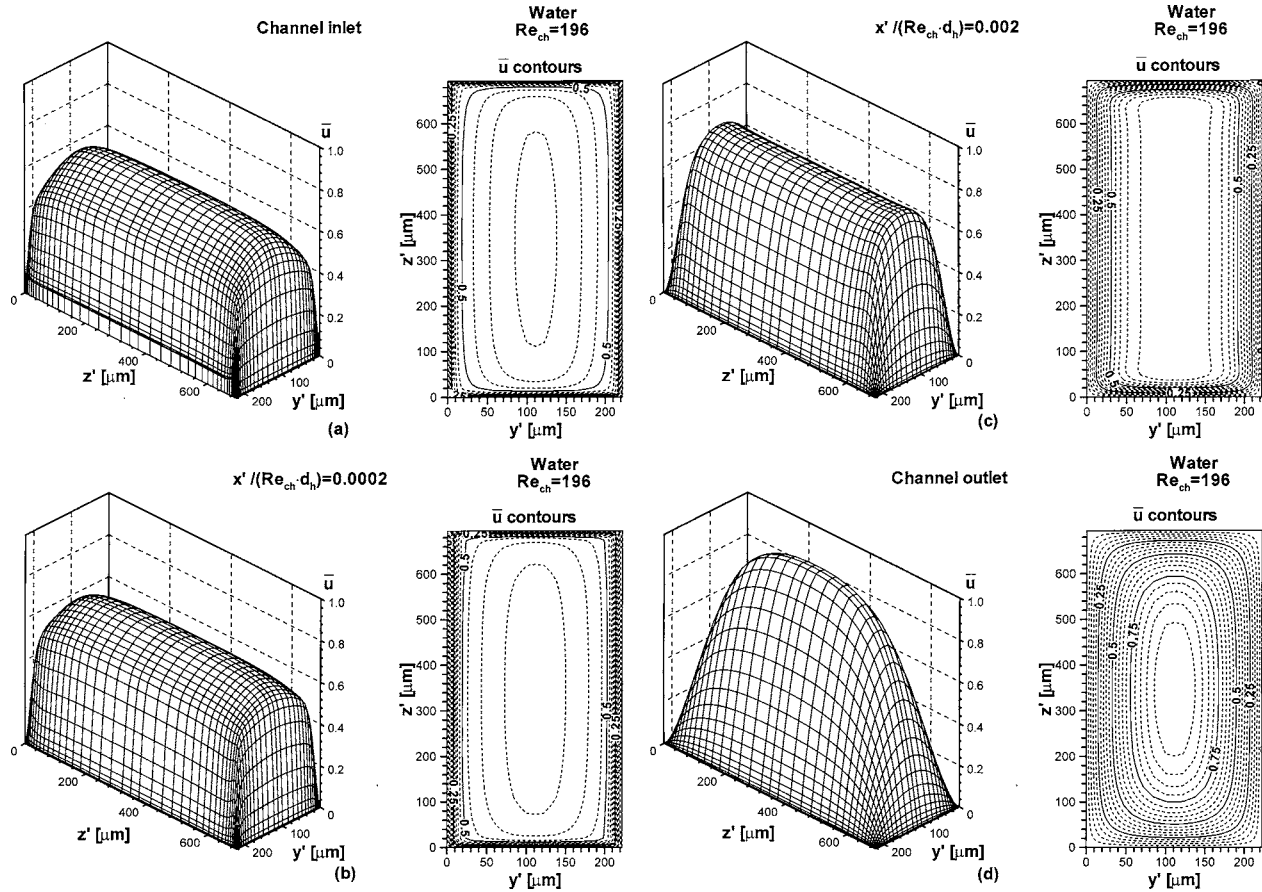
Fig. 10 $\bar{u}$ profile in different y'-z' planes for $Re_{ch}=196$ at (*a*) $x'=0$, (*b*) $x'=0.0002Re_{ch}d_h$, (*c*) $x'=0.002Re_{ch}d_h$, and (*d*) $x' = L_{ch}$

$$Re_{ch} = \frac{\rho_f u_m d_h}{\mu_f} \qquad (9)$$

where u_m is the mean velocity in the micro-channel

$$u_m = \frac{\dot{V}_{exp}}{A_{ch}} \qquad (10)$$

Results and Discussion

Flow Development. Figures 6(*a*) and 6(*b*) compare measured and numerically predicted velocity profiles at two horizontal planes, $z'=347$ and 555 μm, and at a stream-wise position close to the micro-channel inlet, $x'=1$ cm, for $Re_{ch}=196$ and 1895, respectively. Notice that $z'=347$ μm corresponds to the micro-channel's horizontal middle plane, while $z'=555$ μm is in the upper portion of the micro-channel close to the cover plate. Figures 6(*a*) and 6(*b*) show fairly good agreement between the model predictions and micro-PIV data with percentage differences smaller than 3% and 10%, respectively.

Figure 7 shows a similar comparison between measured and predicted velocity profiles at $z'=347$ and 555 μm for $Re_{ch}=1895$ at a downstream location close to the micro-channel outlet, $x'=10$ cm. Fairly good agreement is realized at this downstream location as well with a percentage difference smaller than 9%.

Figure 8 compares the micro-channel central line velocity u_c measured along the stream-wise direction with model predictions for $Re_{ch}=196$ and 1895. Notice that the central line velocity in the inlet shallow plenum is much lower than in the micro-channel because of the much larger flow area of the former. There is a rapid increase in u_c once the flow reaches the micro-channel inlet.

At the relatively high Reynolds number of 1895, u_c shows a significant overshoot and reaches a local maximum within the developing region. This phenomenon is not observed for $Re_{ch}=196$. Figure 8 shows the flow is still developing for $Re_{ch}=1895$ at $x'=1$ cm but fully developed for $Re_{ch}=196$. On the other hand, the flow at $x'=10$ cm is fully developed for both Reynolds numbers. Figure 8 shows fairly good agreement between the model predictions and experimental data for both Reynolds numbers.

The good agreement between the measured and predicted flow velocities in the micro-channel proves the conventional Navier-Stokes equation predicts liquid micro-channel flow fairly accurately.

Figures 9(*a*) and 9(*b*) show non-dimensional $\bar{u}$-$\bar{v}$ vector fields in the middle horizontal plane, $z'=347$ μm, immediately downstream of the micro-channel inlet $(0 \leqslant x'/(Re_{ch}d_h) \leqslant 0.002)$ for $Re_{ch}=196$ and 1895, respectively, where $\bar{u}$ and $\bar{v}$ are nondimensionalized with respect to the centerline velocity at the micro-channel outlet

$$\bar{u} = \frac{u}{u_{c,out}} \quad \text{and} \quad \bar{v} = \frac{v}{u_{c,out}} \qquad (11)$$

When the flow enters the micro-channel from the shallow plenum, the abrupt contraction causes flow separation at the channel inlet and forms vortices near the sidewalls. These vertexes are confined to a short distance from the channel inlet. Comparing Figs. 9(*a*) and 9(*b*) shows the vertexes are more pronounced for $Re_{ch}=1895$, penetrating deeper into the channel, which explains the overshoot in the central line velocity in Fig. 8 for the same Reynolds number.

Figures 10(*a*)–10(*d*) illustrate nondimensional $\bar{u}$ profiles for
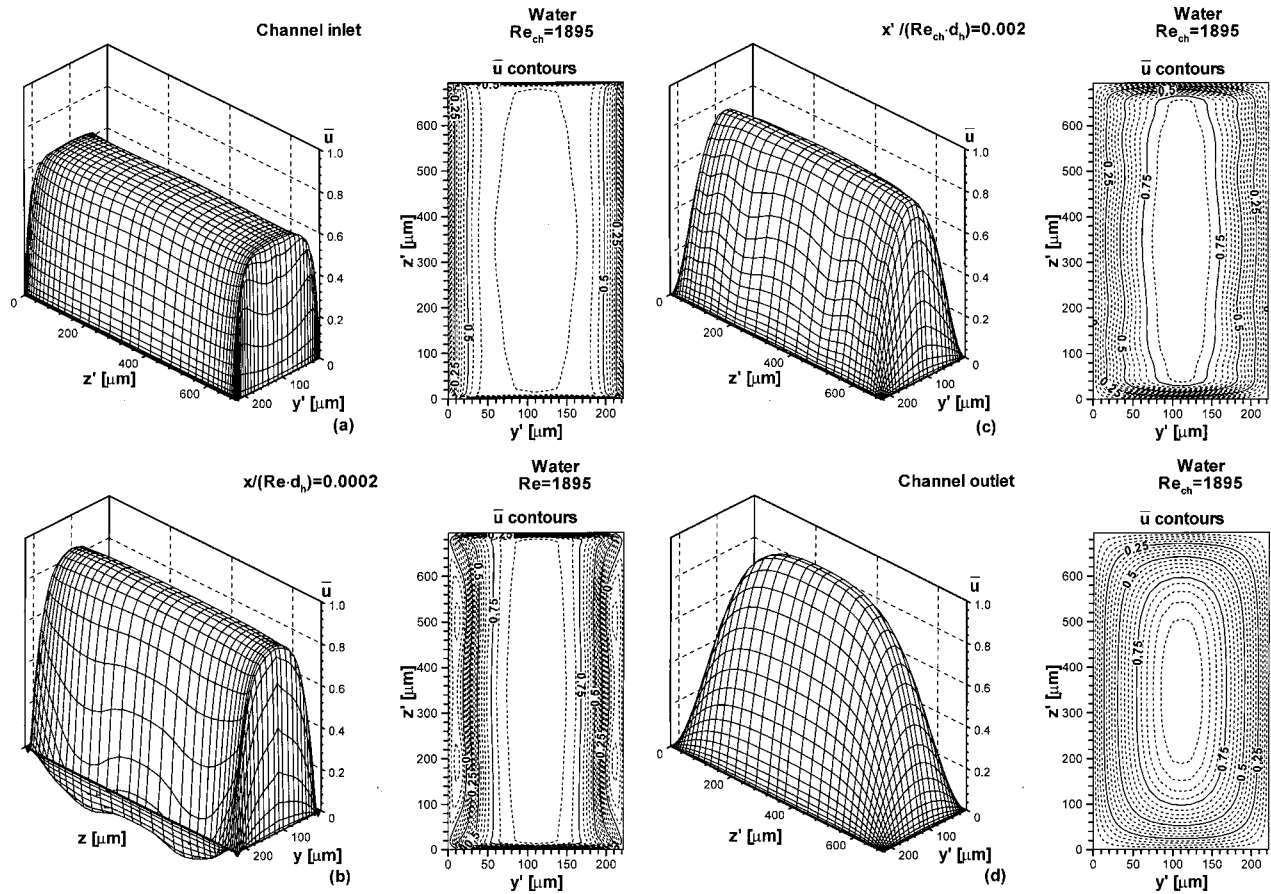
Fig. 11 $\bar{u}$ profile in different y'-z' planes for $Re_{ch}=1895$ at (*a*) $x'=0$, (*b*) $x'=0.0002Re_{ch}d_h$, (*c*) $x'=0.002Re_{ch}d_h$, and (*d*) $x'=L_{ch}$

$Re_{ch}=196$ at four y'-z' planes, $x'=0$, $x'=0.0002Re_{ch}d_h$, $x'=0.002Re_{ch}d_h$, and $x'=L_{ch}$. Similar plots are shown in Figs. 11(*a*)–11(*d*) for $Re_{ch}=1895$. Some interesting features of the flow development are readily observed in these figures. For $Re_{ch}=1895$, four vortices are observed at $x'=0.0002Re_{ch}d_h$, Fig. 11(*b*), and these vortices appear to have a significant effect on the flow development downstream. Overall, flow development is far smoother at $Re_{ch}=196$ than at $Re_{ch}=1895$.

Pressure Drop. The measured pressure drop was compared to predictions based on (*a*) the computational model and (*b*) empirical correlations. The results are shown in Fig. 12 for four Reynolds numbers. Numerical predictions of pressure drop are readily available once Eqs. (3)–(5) are solved numerically. Predictions based on empirical correlations were based on the following relation, which neglects the small pressure drop in the shallow plenums

$$\Delta P_{pred} = \Delta P_{c1} + \Delta P_{c2} + \Delta P_d + \Delta P_{fd} + \Delta P_{e2} + \Delta P_{e1} \qquad (12)$$

where ΔP_{c1} and ΔP_{c2} are the inlet contraction pressure losses, ΔP_{e2} and ΔP_{e1} are the outlet expansion pressure recoveries, and ΔP_d and ΔP_{fd} denote pressure drops in the developing and fully-developed regions. Correlations for the individual pressure drop components in Eqs. (12) are summarized in Table 2 [26,30]. The length of the developing region, L_d, is calculated from Eq. (1), and the length of the fully-developed region, L_{fd}, from

$$L_{fd} = L_{ch} - L_d \qquad (13)$$

Figure 12 shows both the computational model and correlations can adequately predict pressure drop across the micro-channel.

Figure 13 shows numerically predicted pressure distribution along the stream-wise direction for the same four values of Re_{ch}.

The pressure is nearly constant in the inlet and outlet shallow plenums. There is a sudden decrease in pressure immediately after the micro-channel inlet corresponding to the rapid increase in u_c illustrated earlier in Fig. 8. The three larger Reynolds numbers show a local minimum pressure corresponding to the overshoot in u_c.
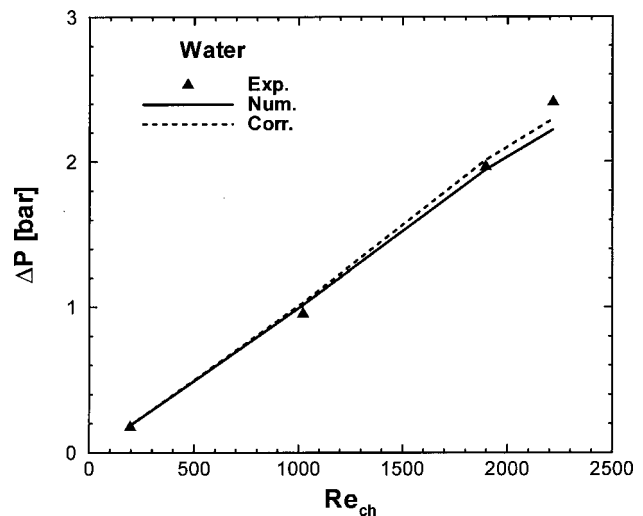
Fig. 12 Comparison of measured pressure drop and predictions based on numerical analysis and correlations for Re_{ch} =196, 1021, 1895, and 2215

Table 2 Micro-channel pressure drop components

ΔP_{c1}, ΔP_{c2}	[30]	$\Delta P_{c1} = \frac{1}{2}\rho_f(u_{p2,\text{in},m}^2 - u_{p1,\text{in},m}^2) + \frac{K_{c1}}{2}\rho_f u_{p2,\text{in},m}^2$ $\Delta P_{c2} = \frac{1}{2}\rho_f(u_m^2 - u_{p2,\text{in},m}^2) + \frac{K_{c2}}{2}\rho_f u_m^2$ $K_{c1} = 0.6740 + 1.2501\beta_{p2} + 0.3417\beta_{p2}^2 - 0.8358\beta_{p2}^3;\ \beta_{p2} = W_{p2}/H_{\text{ch}}$ $K_{c2} = 0.6740 + 1.2501\beta + 0.3417\beta^2 - 0.8358\beta^3;\ \beta = W_{\text{ch}}/H_{\text{ch}}$
ΔP_{e1}, ΔP_{e2}	[30]	$\Delta P_{e2} = \frac{1}{2}\rho_f(u_{p2,\text{out},m}^2 - u_m^2) + \frac{K_{e2}}{2}\rho_f u_m^2$ $\Delta P_{e1} = \frac{1}{2}\rho_f(u_{p1,\text{out},m}^2 - u_{p2,\text{out},m}^2) + \frac{K_{e1}}{2}\rho_f u_{p2,\text{out},m}^2$ $K_{e2} = (1 - A_{\text{ch}}/A_{p2})^2,\ K_{e1} = (1 - A_{p2}/A_{p1})^2$
ΔP_{fd}	[26]	$\Delta P_{\text{fd}} = \frac{2f\rho_f u_m^2 L_{\text{fd}}}{d_h}$ $f\text{Re}_{\text{ch}} = 24(1 - 1.355\beta + 1.947\beta^2 - 1.701\beta^3 + 0.956\beta^4 - 0.254\beta^5)$
ΔP_d	[26]	$\Delta P_d = \frac{2f_{\text{app}}\rho_f u_m^2 L_d}{d_h}$ $f_{\text{app}} = \frac{1}{\text{Re}_{\text{ch}}}\Big[3.44(L_d^+)^{-0.5} + [K(\infty)/(4L_d^+) + f\text{Re}_{\text{ch}} - 3.44(L_d^+)^{-0.5}]/[1 + C(L_d^+)^{-2}]\Big]$ $L_d^+ = L_d/(\text{Re}_{\text{ch}}d_h);\ K(\infty) = 0.6740 + 1.2501\beta + 0.3417\beta^2 - 0.8358\beta^3$ $C = (0.1811 + 4.3488\beta - 1.6027\beta^2) \times 10^{-4}$

Conclusions

Flow development and pressure drop were investigated both experimentally and numerically for adiabatic single-phase water flow in a single 222 μm wide, 694 μm deep, and 12 cm long rectangular micro-channel at Reynolds numbers ranging from 196 to 2215. A micro-PIV system was used to map the velocity field, and pressure drop was measured with the aid of pressure transducers that were situated both upstream and downstream of the micro-channel. A three-dimensional computational model was constructed which provided a detailed description of the liquid velocity field in both the developing and fully developed regions. Key findings from the study are as follows

(1) Fairly good agreement is achieved between the model predictions and measured velocity field both in the developing and fully-developed regions of the micro-channel

(2) At high Reynolds numbers, sharp entrance effects produce pronounced vortices immediately downstream of the inlet. These vortices produce a local maximum in

centerline velocity and local pressure minimum, and have a profound influence on flow development downstream.

(3) The computational model shows excellent agreement with pressure drop measurements. Good agreement is also possible with conventional pressure drop correlations.

(4) This study proves the conventional Navier-Stokes equation accurately predicts liquid flow in micro-channels, and is therefore a powerful tool for the design and analysis of micro-channel heat sinks intended for electronic cooling.

Acknowledgment

Nomenclature

A_{ch} = cross-sectional area of micro-channel
A_{p1} = cross-sectional area of deep plenum
A_{p2} = cross-sectional area of shallow plenum
C = parameter in pressure drop correlation
d_h = hydraulic diameter
f = friction factor
f_{app} = apparent friction factor for developing flow
H_{ch} = height of micro-channel
$K(\infty)$ = entrance loss coefficient
K_{c1}, K_{c2} = contraction loss coefficient
K_{e1}, K_{e2} = expansion recovery coefficient
L_{ch} = length of micro-channel
L_d^+ = Nondimensional length of developing region
L_d = length of developing region
L_{fd} = length of fully developed region
L_{p2} = length of shallow plenums
P = pressure
ΔP = pressure drop across micro-channel
$\Delta P_{c1}, \Delta P_{c2}$ = contraction pressure loss
$\Delta P_{e1}, \Delta P_{e2}$ = expansion pressure recovery
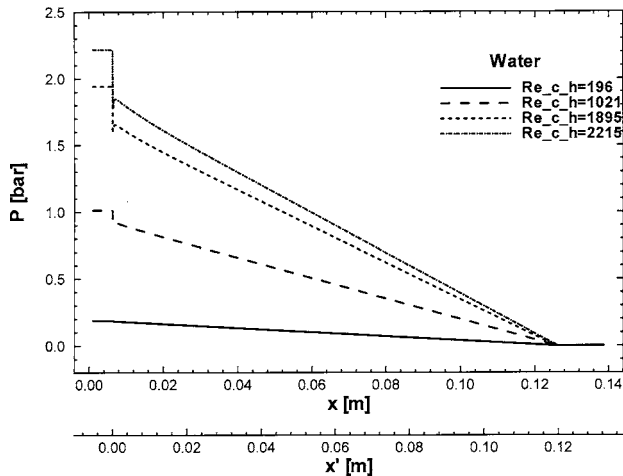
Fig. 13 Numerically predicted variation of pressure along stream-wise direction for $\text{Re}_{\text{ch}} = 196$, 1021, 1895, and 2215

ΔP_d = pressure drop in developing region
ΔP_{fd} = pressure drop in fully-developed region
Re = Reynolds number
u = velocity component in x direction
u_c = central line velocity
u_m = mean velocity in micro-channel
$\bar{u}$ = nondimensional velocity component in x direction
v = velocity component in y direction
$\bar{v}$ = nondimensional velocity component in y direction
$\dot{V}$ = volume flow rate
w = velocity component in z direction
W_{p2} = width of shallow plenum
x,y,z = full domain coordinates
x',y',z' = micro-channel coordinates

Greek Symbols

β = aspect ratio
μ = viscosity
ρ = density
τ = iteration number

Subscripts

ch = channel; micro-channel
d = developing region
exp = measured
f = fluid
fd = fully developed region
in = inlet
m = average
out = outlet
pred = predicted
$p1$ = deep plenum
$p2$ = shallow plenum

References

[1] Mudawar, I., 2001, "Assessment of High-Heat-Flux Thermal Management Schemes," IEEE Trans. Compon. Packag. Technol., **24**, pp. 122–141.
[2] El-Masri, M. A., and Louis, J. F., 1978, "On the Design of High-Temperature Gas Turbine Blade Water-Cooled Channels," ASME J. Eng. Power, **100**, pp. 586–591.
[3] Mudawar, I., El-Masri, M. A., Wu, C. S., and Ausman-Mudawar, J. R., 1985, "Boiling Heat Transfer and Critical Heat Flux in High-Speed Rotating Films," Int. J. Heat Mass Transfer, **28**, pp. 795–806.
[4] Tuckerman, D. B., and Pease, R. F. W., 1981, "High-Performance Heat Sinking for VLSI," IEEE Electron Device Lett., **2**, pp. 126–129.
[5] Ravigururajan, T. S., Cuta, J., McDonald, C. E., and Drost, M. K., 1996, "Single-Phase Flow Thermal Performance Characteristics of a Parallel Micro-Channel Heat Exchanger," *Proceedings of National Heat Transfer Conference*, Vol. 7, ASME HTD-329, pp. 157–166.
[6] Harms, T. M., Kazmierczak, M. J., and Cerner, F. M., 1999, "Developing Convective Heat Transfer in Deep Rectangular Microchannels," Int. J. Heat Fluid Flow, **20**, pp. 149–157.
[7] Rahman, M. M., 2000, "Measurements of Heat Transfer in Microchannel Heat Sinks," Int. Commun. Heat Mass Transfer, **27**, pp. 495–506.
[8] Kawano, K., Minakami, K., Iwasaki, H., and Ishizuka, M., 1998, "Micro Channel Heat Exchanger for Cooling Electrical Equipment," *Proceedings of the ASME Heat Transfer Division*, R. A. Nelson, L. W. Swanson, M. V. A. Bianchi, C. Camci, eds., Vol. 3, HTD-Vol.361-3/PID, pp. 173–180.
[9] Qu, W., and Mudawar, I., 2002, "Experimental and Numerical Study of Pressure Drop and Heat Transfer in a Single-Phase Micro-Channel Heat Sink," Int. J. Heat Mass Transfer, **45**, pp. 2549–2565.
[10] Knight, R. W., Goodling, J. S., and Hall, D. J., 1991, "Optimal Thermal Design of Forced Convection Heat Sinks—Analytical," ASME J. Electron. Packag., **113**, pp. 313–321.
[11] Knight, R. W., Hall, D. J., Goodling, J. S., and Jaeger, R. C., 1992, "Heat Sink Optimization With Application to Microchannels," IEEE Trans. Compon., Hybrids, Manuf. Technol., **15**, pp. 832–842.
[12] Lee, D. Y., and Vafai, K., 1999, "Comparative Analysis of Jet Impingement and Microchannel Cooling for High Heat Flux Applications," Int. J. Heat Mass Transfer, **42**, pp. 1555–1568.
[13] Choquette, S. F., Faghri, M., Charmchi, M., and Asako, Y., 1996, "Optimum Design of Microchannel Heat Sinks," *Micro-Electro-Mechanical Systems (MEMS) - 1996*, DSC-Vol. 59, ASME, New York, pp. 115–126.
[14] Fedorov, A. G., and Viskanta, R., 2000, "Three-Dimensional Conjugate Heat Transfer in the Microchannel Heat Sink for Electronic Packaging," Int. J. Heat Mass Transfer, **43**, pp. 399–415.
[15] Qu, W., and Mudawar, I., 2002, "Analysis of Three-Dimensional Heat Transfer in Micro-Channel Heat Sinks," Int. J. Heat Mass Transfer, **45**, pp. 3973–3985.
[16] Peng, X. F., Peterson, G. P., and Wang, B. X., 1994, "Frictional Flow Characteristics of Water Flowing Through Rectangular Microchannels," Exp. Heat Transfer, **7**, pp. 249–264.
[17] Mala, G. M., and Li, D., 1999, "Flow Characteristics of Water in Microtubes," Int. J. Heat Fluid Flow, **20**, pp. 142–148.
[18] Papautsky, I., Brazzle, J., Ameel, T., and Frazier, A. B., 1999, "Laminar Fluid Behavior in Microchannels Using Micropolar Fluid Theory," Sens. Actuators, A, **A73**, pp. 101–108.
[19] Qu, W., Mala, G. M., and Li, D., 2000, "Pressure-Driven Water Flow in Trapezoidal Silicon Microchannels," Int. J. Heat Mass Transfer, **43**, pp. 353–364.
[20] Pfahler, J., Harley, J., Bau, H. H., and Zemel, J. N., 1990, "Liquid Transport in Micron and Submicron Channels," Sens. Actuators, A, **A21–A23**, pp. 431–434.
[21] Choi, S. B., Barron, R. R., and Warrington, R. O., 1991, *Fluid Flow and Heat Transfer in Micro Tubes*, ASME DSC Vol. 40, pp. 89–93.
[22] Yu, D., Warrington, R. O., Barron, R. R., and Ameel, T., 1995, "An Experimental and Theoretical Investigation of Fluid Flow and Heat Transfer in Microtubes," *ASME/JSME Thermal Engineering Conference*, Vol. 1, pp. 523–530.
[23] Flockhart, S. M., and Dhariwal, R. S., 1998, "Experimental and Numerical Investigation into the Flow Characteristics of Channels Etched in ⟨100⟩ Silicon," ASME J. Fluids Eng., **120**, pp. 291–295.
[24] Judy, J., Maynes, D., and Webb, B. W., 2002, "Characterization of Frictional Pressure Drop for Liquid Flows through Microchannels," Int. J. Heat Mass Transfer, **45**, pp. 3477–3489.
[25] Wu, H. Y., and Cheng, D., 2003, "Friction Factors in Smooth Trapezoidal Silicon Microchannels With Different Aspect Ratios," Int. J. Heat Mass Transfer, **46**, pp. 2519–2525.
[26] Shah, R. K., and London, A. L., 1978, *Laminar Flow Forced Convection in Ducts: A Source Book for Compact Heat Exchanger Analytical Data*, Academic, New York, Supl. 1.
[27] Qu, W., and Mudawar, I., 2003, "Thermal Design Methodology for High-Heat-Flux Single-Phase and Two-Phase Micro-Channel Heat Sinks," IEEE Trans. Compon. Packag. Technol., **26**, pp. 598–609.
[28] Lee, S. Y., Wereley, S. T., Gui, L., Qu, W., and Mudawar, I., 2002, "Microchannel Flow Measurements Using Micro Particle Image Velocimetry," *Proceedings of the ASME Fluid Engineering Division-2002*, ASME, New York, FED-Vol. 258, A. Ognut, ed., pp. 493–500.
[29] Patankar, S. V., 1980, *Numerical Heat Transfer and Fluid Flow*, Hemisphere, Washington, D.C.
[30] Blevins, R. D., 1984, *Applied Fluid Dynamics Handbook*, Van Nostrand Reinhold, New York.